Full Length Article

Three-dimensional porous activated carbon derived from loofah sponge biomass for supercapacitor applications

Xiao-Li Su [a], Jing-Ran Chen [a], Guang-Ping Zheng [b], Jing-He Yang [c],[**], Xin-Xin Guan [a],[d], Pu Liu [a], Xiu-Cheng Zheng [a],[d],[*]

[a] College of Chemistry and Molecular Engineering, Zhengzhou University, Zhengzhou 450001, China
[b] Department of Mechanical Engineering, The Hong Kong Polytechnic University, Hong Kong, China
[c] School of Chemical Engineering and Energy, Zhengzhou University, Zhengzhou 450001, China
[d] Key Laboratory of Advanced Energy Materials Chemistry (Ministry of Education), Nankai University, Tianjin 300071, China

A B S T R A C T

Biomass carbon source is generally cheap, environmentally friendly and readily available in high quality and quantity. In this work, a series of loofah sponge-derived activated carbon (SAC-*x*) with hierarchical porous structures are prepared by KOH chemical activation and used as electrode materials for supercapacitors. The pore size can be easily controllable by changing the dosage of KOH. The optimized material (SAC-4) exhibits a high specific capacitance of $309.6\,F\,g^{-1}$ at $1\,A\,g^{-1}$ in the three-electrode system using $6\,M$ KOH electrolyte. More importantly, the as-assembled symmetric supercapacitor based on SAC-4 exhibits a high energy density of $16.1\,Wh\,kg^{-1}$ at a power density of $160.0\,W\,kg^{-1}$ using $1\,M\,Na_2SO_4$ electrolyte. These remarkable results demonstrate the exciting commercial potential of SAC-*x* for high-performance supercapacitor applications due to their high specific surface area, appropriately porous structure, and the trace heteroatom (O and N) functionalities.

© 2017 Elsevier B.V. All rights reserved.

1. Introduction

Electrochemical capacitors, also known as supercapacitors, are promising energy storage devices and have drawn much attention owing to their unique properties including fast charge-discharge, high power density and long lifecycle [1–3]. They have been extensively applied in various fields such as portable electrons, digital communication, hybrid electrical vehicles and renewable energy systems [3–7].

According to the charge storage mechanisms, supercapacitors can be classified into two basic types: (1) Electric double layer capacitors (EDLCs), in which the charge storage is achieved by the adsorption of ionic species and charged particles at the electrode/electrolyte interfaces, and (2) Pseudocapacitors, which arises from the Faradaic redox reactions between the electrolyte and electro-active surfaces of the electrode materials [1–11]. Compared with EDLCs, in spite of much higher specific capacity for redox reactions with an array of oxidation states, the commercial applications of the pseudo-capacitive materials are limited due to the weak electrical conductance, poor compatibility and narrow potential windows with organic electrolytes. In addition, the short cycle life of the pseudocapacitors also limits their practical applications [9,12]. Therefore, it is urgent to develop electrode materials for high-performance EDLCs.

Remarkably, carbon based materials (carbon nanotubes, carbon nanofibers, and activated carbons, etc.) are considered as ideal electrode materials for EDLCs because of their distinct characteristics such as controlled porous structure, high conductivity, and large surface area [13,14]. Among them, the renewable biomass-derived activated carbons are of particular interest since they contain abundant cellulose, hemicellulose, and lignin, which yield favorable capacitive properties and provide a sustainable resource for the production of carbon-based energy devices [15]. Moreover, the biomass-derived carbons are relatively less expensive, and have high specific surface areas, excellent chemical stability and good environmental compatibility [16].

As one of the sustainable and renewable biomass materials, loofah sponge (the dry skeleton of loofah) consists of intercon-

* Corresponding author at: College of Chemistry and Molecular Engineering, Zhengzhou University, Zhengzhou 450001, China.
** Corresponding author.
E-mail addresses: jhyang@zzu.edu.cn (J.-H. Yang), zhxch@zzu.edu.cn (X.-C. Zheng).

nected plant fibers, which is mainly composed of lignin and various kinds of cellulose with elements of C, H, O and N [17,18]. Furthermore, it has a natural porous network structure composed of tens or hundreds of interconnected bundled microtubes. This unique structure can be well kept after carbonation. Hence, loofah sponge-derived carbon materials have been used as a highly conductive matrix for MoS_2 in sodium ion batteries [17], blocking layers for high performance rechargeable lithium batteries [18], and electrode materials for supercapacitors [19–21]. Even so, to the best of our knowledge, there is little literature on the loofah sponge-derived carbons chemically activated with various KOH dosages.

In this work, loofah sponge-derived activated carbons with hierarchical porous structure are prepared by a facile procedure including drying, carbonization, KOH chemical activation, and acid/water washing. The unique advantages of the synthetic strategy are as follows: (I) Naturally sustainable loofah sponge containing a large amount of functional group is served as carbon precursor; (II) The porous structure can be controlled by adjusting the dosage of KOH. As electrode materials for supercapacitors, the activated carbons are expected to decrease the ion transport resistance and diffusion distance in the charge storage devices because of their unique architectures, resulting in improved capacitive performance.
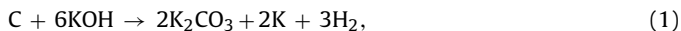
2. Experiments

2.1. Preparation of the activated carbon materials

The schematic illustration for the preparation of porous loofah sponge-derived activated carbons is shown in Fig. 1. Firstly, a certain amount of loofah sponge were cut into small pieces, washed with DI water to remove the impurities and then dried at 110 °C overnight. Subsequently, the loofah sponge was calcined at 600 °C for 4 h at a heating rate of 2 °C min^{-1} under nitrogen atmosphere in a tubular furnace. The resulting material was denoted as SC.

SC was further immersed into KOH solution with various mass ratios of KOH to SC. After drying at 110 °C, the material was activated at 800 °C for 1 h with a heating rate of 3 °C min^{-1} under nitrogen atmosphere in a tubular furnace. Finally, the products were dispersed into adequate HCl solution (1.0 mol L^{-1}) to consume K produced in the aforementioned chemical activation procedures and the residual KOH. Then, the resulting KCl and the residual HCl in the solution were washed with DI water, which was subsequently dried at 110 °C. The as-prepared materials were denoted as SAC-x, where x represented the mass ratio of KOH to SC (x = 0.5, 1, 2, 4, 6, and 8, respectively). The chemical reactions in the activation procedure were as follows (Eqs. (1)–(6)) [12,25]:

$$C + 6KOH \rightarrow 2K_2CO_3 + 2K + 3H_2, \tag{1}$$

$$K_2CO_3 \rightarrow K_2O\,CO_2, \tag{2}$$

$$K_2CO_3 + 2C \rightarrow 2K + 3CO, \tag{3}$$

$$K_2O + C \rightarrow 2K + 3CO, \tag{4}$$

$$2K + 2H_2O \rightarrow 2KOH + H_2, \tag{5}$$

$$KOH + HCl \rightarrow KCl + H_2O. \tag{6}$$

2.2. Characterization

The electronic microscopy studies on the samples were performed using a Zeiss Ultra 55 scanning electron microscope (SEM) and a FEITalos F200S transmission electron microscope (TEM). The textural parameters of the samples were obtained from nitrogen adsorption-desorption isotherms at −196 °C using a Micromeritics ASAP 2420-4MP automated surface area and pore size analyzer. The materials were degassed at 250 °C for 3 h and the Brunaueree-Emmettee-Teller (BET) method was used to calculate the specific surface area. The density functional theory (DFT) model assuming cylindrical-shaped pores was utilized to obtain the pore-size distribution (PSD). The phase structures were determined by X-ray diffraction (XRD) on a Panalytical X'pertPro diffractometer operated at 40 kV and 40 mA using Cu Kα radiation (λ = 0.1546 nm). Surface chemistry was investigated by X-ray photoelectron spectroscopy (XPS) using an RBD upgraded PHI-5000C ESCA system (Perkin Elmer) and the binding energies were calibrated using the containment carbon (C 1s = 284.6 eV).

2.3. Electrochemical measurements

The capacitive performances of the resulting activated carbon materials were evaluated using a three-electrode system and a symmetrical two-electrode system, respectively.

In the three-electrode system, the working electrode was prepared by mixing the carbon materials with 10 wt% acetylene black and 10 wt% polytetrafluoroethylene (PTFE), and pressing the mixture onto nickel foam (1 cm × 1 cm) with a mass loading of 2–3 mg.
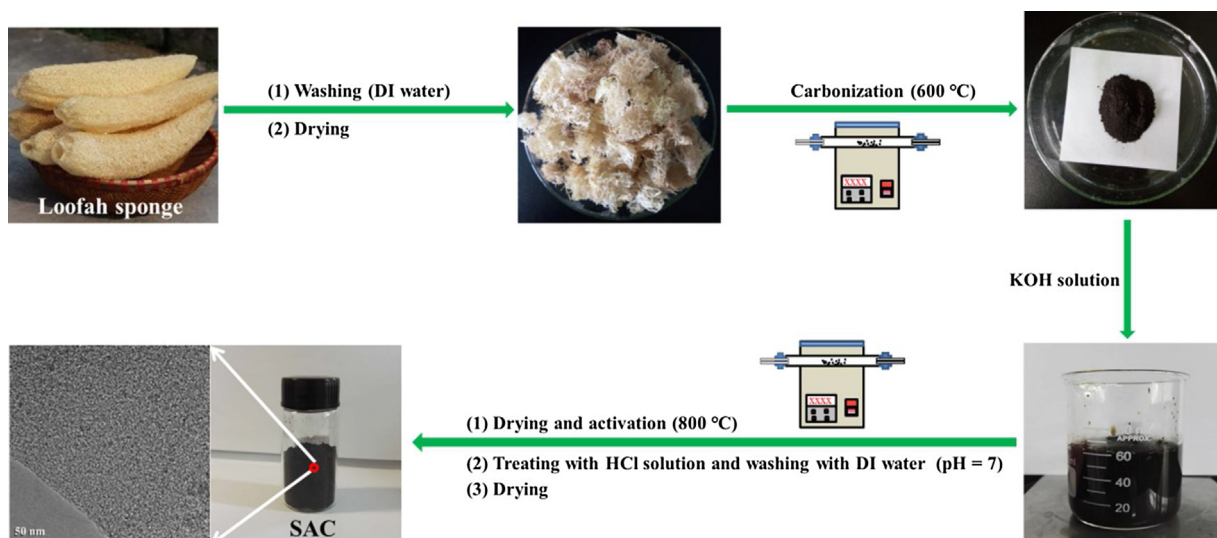

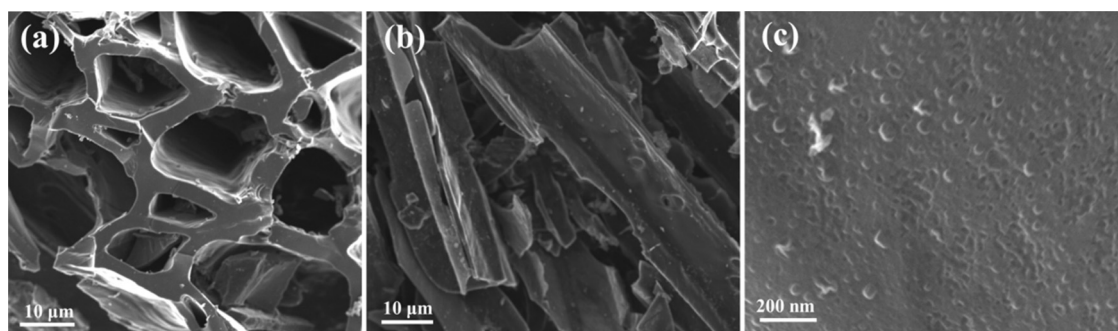**Fig. 1.** Schematic illustration for the preparation of SAC-x.

Fig. 2. SEM images of SAC-4.

A platinum wire and a saturated calomel electrode were served as the counter electrode and the reference electrode, respectively. A KOH aqueous solution (6 M) was used as electrolyte. Cyclic voltammetry (CV), galvanostatic charge-discharge (GCD), and electrochemical impedance spectroscopy (EIS) measurements were performed with a CHI 660E electrochemical workstation. EIS was performed in the frequency ranging from 10 kHz to 10 mHz at the open circuit voltage with an alternate current amplitude of 5 mV. The CV measurements were performed from 0 to −1.0 V at different constant scan rates (5–100 mV s^{-1}).

The symmetrical supercapacitors were prepared based on a CR2032 stainless steel coin cell. The cell was assembled with two circular nickel foam electrodes with a diameter of 1 cm, which have the same amount of loaded materials. The electrodes were separated with a polypropylene separator and soaked with 1 M Na_2SO_4 electrolyte. The cyclic voltammetry of symmetrical cell devices was studied within a potential range of 0–1.6 V.

The specific capacitance (C_m, Fg^{-1}) of the supercapacitors was calculated from the charge-discharge profiles using Eq. (7) [22],

$$C_m = \frac{I_d \times \Delta t}{\Delta V \times m}. \tag{7}$$

where I_d (mA) was the constant discharge current, Δt (s) was the discharge time, and ΔV (V) was the potential discharge voltage range. m (mg) was the mass of active materials in the working electrode.

The specific energy density (E, Wh kg^{-1}) and specific power density (P, W kg^{-1}) of the symmetrical supercapacitor system were calculated using Eqs. (8) and (9), respectively [22].

$$E = \frac{1}{2} C_m \times V^2, \tag{8}$$

$$P = \frac{E}{t}. \tag{9}$$

Where V (V) was the cell-operation potential and t (h) was the discharge time.

3. Results and discussion

3.1. Characterization

In order to clearly reveal the microstructures of SAC-x, SEM analysis on SAC-4 is carried out. As shown in Fig. 2a and b, the typical SAC-4 material shows a 3D network structure consisting of a large amount of cross-linked hollow microtubes whose tube wall thickness is around 2 μm. The high-magnification SEM image of SAC-4 shown in Fig. 2c reveals that there are some pores with diameters of tens of nanometers on the walls, which could come from the pyrolysis of loofah sponge because of the evaporation of H_2O, CO_2 and H_2 during the calcination procedure. Since the micropores created by KOH etching could not be easily observed in SEM

images, TEM analysis on SC and SAC-4 are comparatively performed (Fig. 3). Compared with the loose surfaces without obvious pores of SC shown in Fig. 3a and b, abundant microrpores or mesopores resulting from the chemical activation of KOH can be observed in the TEM images of SAC-4 (Fig. 3d and e). In other words, the macropores, mesopores produced by the pyrolysis of loofah sponge and micropores produced by the chemical activation of KOH suggest that SAC-4 has a hierarchical porous structure. Such porous structure is suitable for the rapid diffusion of electrolyte ions into the interiors of SAC-4 during the charge-discharge process through the interconnected and low-resistance channels when SCA-4 is used as electrode materials for supercapacitors [19]. The hierarchical porous structures are further characterized by high-resolution TEM images. From Fig. 3c and f, we can observe that both SC and SAC-4 have a disordered texture structure and there exist ribbons with some degrees of graphitization. The fringes for SAC-4 are obviously obscurer than that for SC, indicating that the activation of KOH increases the structural disorder due to the formation of pores. In addition, the selected area electron diffraction (SAED) patterns for SC and SAC-4 demonstrate their amorphous nature (insets of Fig. 3c and f).

The crystal structures of SC and SAC-x are further confirmed by XRD analysis (Fig. 4). All the materials exhibit two broad peaks at around 22° and 43.9° corresponding to the diffractions of (002) and (100) planes of graphitic frameworks [23]. Furthermore, it is obviously observed the peaks are broadened and their intensities decrease with increasing x (the mass ratio of KOH to SC), especially for the (100) diffraction peak. The results demonstrate that the KOH etching reduces the regularity of the structure of SC because of the formation of pores or defects, which are similar with those reported in literature [24].

Raman spectra for the resulting materials shown in Fig. 5 display two prominent peaks at ca. 1329 cm^{-1} (D band) and 1587 cm^{-1} (G band), suggesting the crystallography and structure of the carbon materials. The intensity ratio of D band to G band (I_D/I_G) increases with increasing of the dosage of KOH, implying that the SAC-x has more disordered and defective carbons than SC. This is consisted with the aforementioned analytic results of TEM and XRD.

N_2 adsorption-desorption analysis is performed to investigate the porosity of the as-prepared materials. As shown in Fig. 6a, unlike SC which presents a type-VI isotherm with an obvious type-H4 hysteresis loop typical for narrow slit-like pores [25], which is also individually shown in Fig. S1 (Supplementary material), all the SAC-x materials possess high N_2 sorption capacity and display a type-I sorption isotherm characteristic. The steep increase in volume adsorbed occurs at low relative pressure ($P/P_0 < 0.05$), indicating the presence of abundant micropores (pore width < 2 nm) [26]. It distinctly illustrates the number of micropore increases with the dosage of KOH from $x = 0.5$ to 4 while the micropore decreases when x further increases to 6 and 8. Furthermore, the pore size distribu-
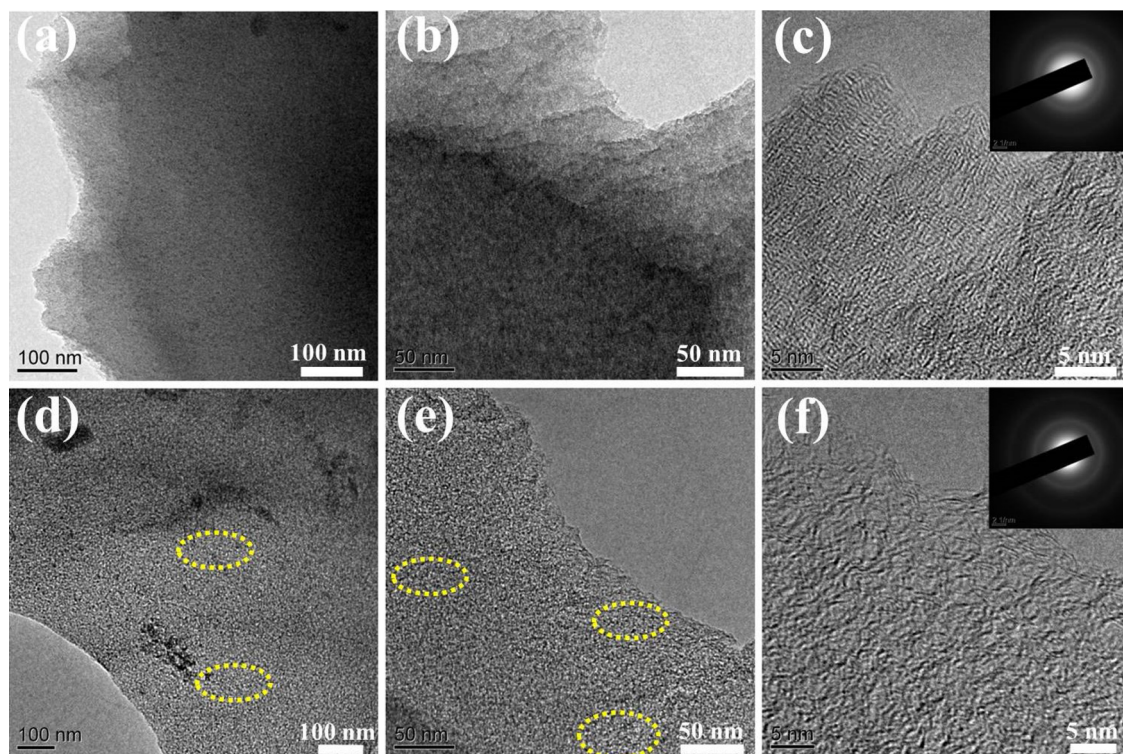
Fig. 3. TEM images of SC (a–c) and SAC-4 (d–f); SAED patterns of SC (inset of c) and SAC-4 (inset of f).
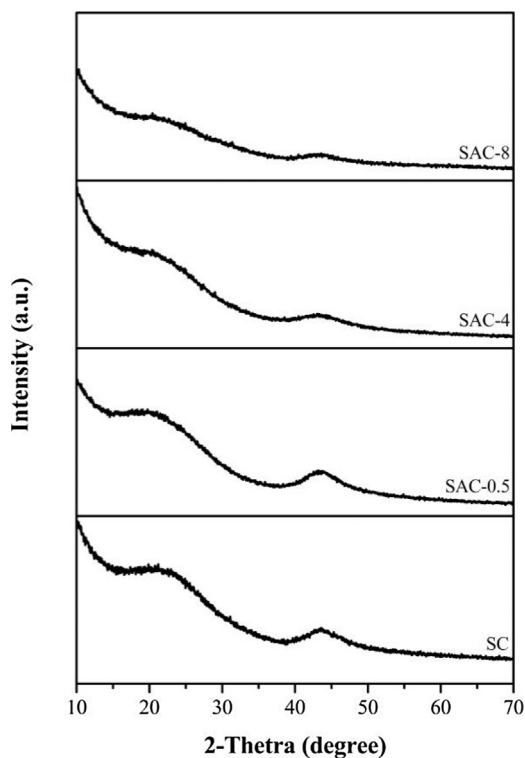

Fig. 4. XRD patterns for SC and SAC-x.

Fig. 5. Raman spectra of SC and SAC-x.

Table 1
Characteristics of porous SC and SAC-x.

Material	S_{BET}[a] ($m^2\,g^{-1}$)	V_p[b] ($cm^3\,g^{-1}$)	D_a[c] (nm)
SC	28	0.037	5.39
SAC-0.5	1531	0.701	1.83
SAC-4	2718	1.503	2.21
SAC-8	2291	1.222	2.13

[a] S_{BET}, specific surface area calculated by the BET method.
[b] V_p, total pore volume determined by N_2 adsorption at a relative pressure of 0.99.
[c] D_a, adsorption average pore width.

tion reveals that the micro-mesopores (with sizes of 0.5–3.5 nm) of SAC-4 have a broader size distribution than those of SAC-0.5 and SAC-8 (Fig. 6b). Notably, no obvious pore size distribution could be found for SC.

Table 1 reveals that the specific surface areas of SAC-x are much higher than that of SC (28 $m^2\,g^{-1}$). As for SAC-x, the value increases with increasin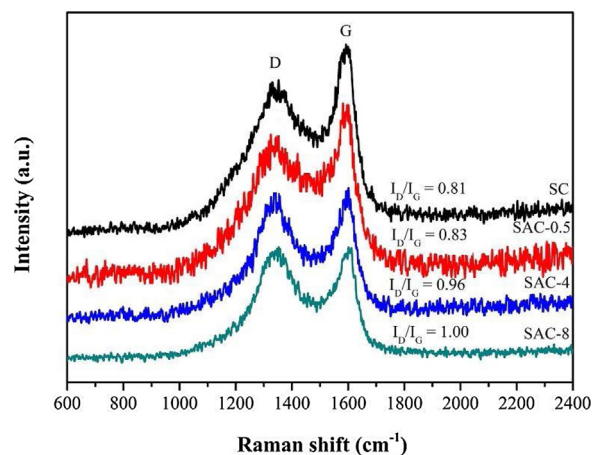g x to some extent due to the formation of pores by KOH etching, while SAC-4 is an exception. As listed in Table 1, the specific surface area of SAC-4 (2718 $m^2\,g^{-1}$) is not only higher than that of SAC-0.5 (1531 $m^2\,g^{-1}$), but also higher than that of SAC-8 (2291 $m^2\,g^{-1}$). This feature of SAC-4 could be related to the fact that the excessive activation of loofah sponge-derived carbon by high
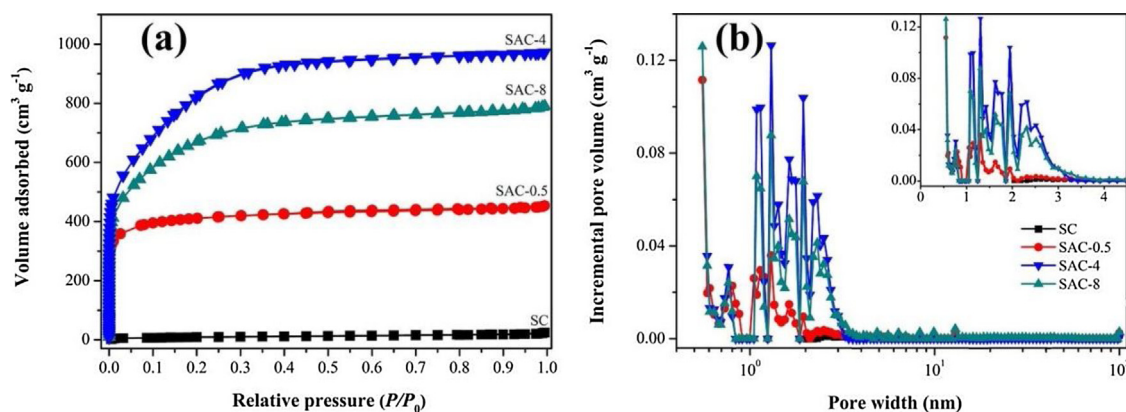
Fig. 6. N$_2$ adsorption-desorption isotherms (a) and pore size distributions (b) for SC and SAC-x.

KOH dosage causes the collapse of etching pores and leads to the decrease of specific surface area. Similar results have been reported for the eulaliopsis binata-derived [25] and tofu-derived [26] carbon materials. Meanwhile, the total pore volume of SAC-4 (1.503 cm^3 g^{-1}) is also higher than those of SAC-8 (1.222 cm^3 g^{-1}), SAC-0.5 (0.701 cm^3 g^{-1}) and SC (0.037 cm^3 g^{-1}). In general, SAC-4 possesses the highest specific surface area and pore volume as well as the most abundant pores among the materials, which are considered as important features of electrode materials in supercapacitors.

The elemental composition and chemical bonding states on the surface of SAC-4 are further investigated by XPS. The full scan spectrum shown in Fig. 7a indicate that SAC-4 mainly contains C (80.8 at%), O (18.1 at%) and N (1.1 at%) elements. The decomposition of C 1s spectrum reveals three peaks, namely, those for O=C—O, C=N, and C=C at 289.4, 285 and 284.6 eV, respectively (Fig. 7b). The O 1s spectrum shown in Fig. 7c is fitted into two peaks at 531.2 eV and 534.0 eV, referring to C=O and C—O bonds, respectively. The N 1s peaks can be assigned to pyridine-N-oxyde (402.7 eV), pyrrolic/pyridone-N (400.2 eV) and pyridinic-nitrogen (398.3 eV), as shown in Fig. 7d. The poor signal of N 1s is attributed to its low content in this material (1.1 at%). It is reported that the pyridinic-N and pyrrolic/pyridone-N are considered to be electrochemically active in an alkaline aqueous solution, which can create defects to provide more open channels and active sites and thus induce the pseudo-capacitance [14,27]. In conclusion, the co-existence of nitrogen- and oxygen- containing functionalities not only provides SAC-4 with some acid-base characteristics which would increase the surface area accessible to aqueous electrolyte, but also results in extra pseudo-capacitance [28,29]. Those advantages will be in favor of SAC-4 to add extra electrochemical capacitance.

3.2. Electrochemical performance

3.2.1. Electrochemical performance in the three-electrode system

The electrochemical properties of the resulting electrode materials are firstly evaluated in the three-electrode system. Fig. 8a shows the CV curves for the electrodes at a scan rate of 100 mV s^{-1}. The curves exhibit an approximately rectangular shape, showing a double-layer capacitance behavior. The hump at high voltages ranging from −0.4 V to 0 V is caused by the redox reactions due to the existence of nitrogen and oxygen functional groups, as mentioned above. Moreover, it is obvious that the area of CV curve for SAC-4 is much larger than those for SC and other SAC-x samples, implying that SAC-4 possesses the highest capacitance.

The CV curves for SAC-4 at different scan rates (5–100 mV s^{-1}) are shown in Fig. 8b. The rectangular shape is also maintained even

Table 2
Comparison on specific capacitances of biomass-based carbon materials.

Material	C_m (F g^{-1}) (current density)	Electrolyte	Ref.
Stiff silkworm	304 (1 A g^{-1})	6 M KOH	[12]
Willow Catkin	292 (1 A g^{-1})	6 M KOH	[13]
Poplar catkin	314.6 (0.5 A g^{-1})	6 M KOH	[22]
Willow catkin	340 (0.1 A g^{-1})	6 M KOH	[24]
Stem bark of broussonetia papyrifera	320 (0.5 A g^{-1})	6 M KOH	[28]
Bagasse	320 (0.5 A g^{-1})	6 M KOH	[31]
Potato waste residue	255 (0.5 A g^{-1})	2 M KOH	[32]
Acacia gum	272 (1 A g^{-1})	6 M KOH	[34]
Chicken eggshell membrane	297 (0.2 A g^{-1})	1 M KOH	[35]
Shiitake mushroom	306 (1 A g^{-1})	6 M KOH	[36]
SCA-4	309.6 (1 A g^{-1})	6 M KOH	This work

at 100 mV s^{-1}. This is mainly ascribed to the unique hierarchical porous structure containing abundant sites, which could facilitate the surface adsorption-desorption within micropores, fast ionic transportation in channels within the mesopores, and short diffusion distance from mesopores to micropores for electrolyte ions [30,31].

Fig. 8c presents the GCD curves for SC and SAC-x at a current density of 3 A g^{-1}. The curves exhibit a shape of isosceles triangle, indicating the good capacitive behavior of EDLCs. The slight distortion may be resulted from the pseudo-capacitance generated by those heteroatom (N and O) containing functional groups. According to Eq. (7), the specific capacitances are 56.3, 181.7, 239.8, 309.6, 251.6 and 222.3 F g^{-1} for SC, SAC-0.5, SAC-2, SAC-4, SAC-6 and SAC-8, respectively. The specific capacitances of SAC-x are much higher than that of SC due to their porous structures activated by KOH, which enhance the kinetics of ion and electron transport in the electrodes and at the electrode/electrolyte interfaces [32]. Remarkably, SAC-4 shows obviously longer discharge time than the others, meaning that it has the largest specific capacitance. As mentioned above, the large specific capacitance might be attributed to its high specific surface area and total pore volume. Moreover, some specific surface areas of SCA-4 are underestimated since lots of extremely small micropores (≪1 nm) could not be effectively detected by N$_2$ but could be accessible by K$^+$ (0.31 nm) and OH$^-$ (0.35 nm), which significantly enhance the double-layer capacitance [33]. As listed in Table 2, SAC-4 exhibits a specific capacitance nearly comparable to or even higher than those of other biomass-derived carbon materials reported in literature.

The GCD curves for SAC-4 electrode at different current densities are shown in Fig. 8d. The nearly symmetric and linear GCD curves
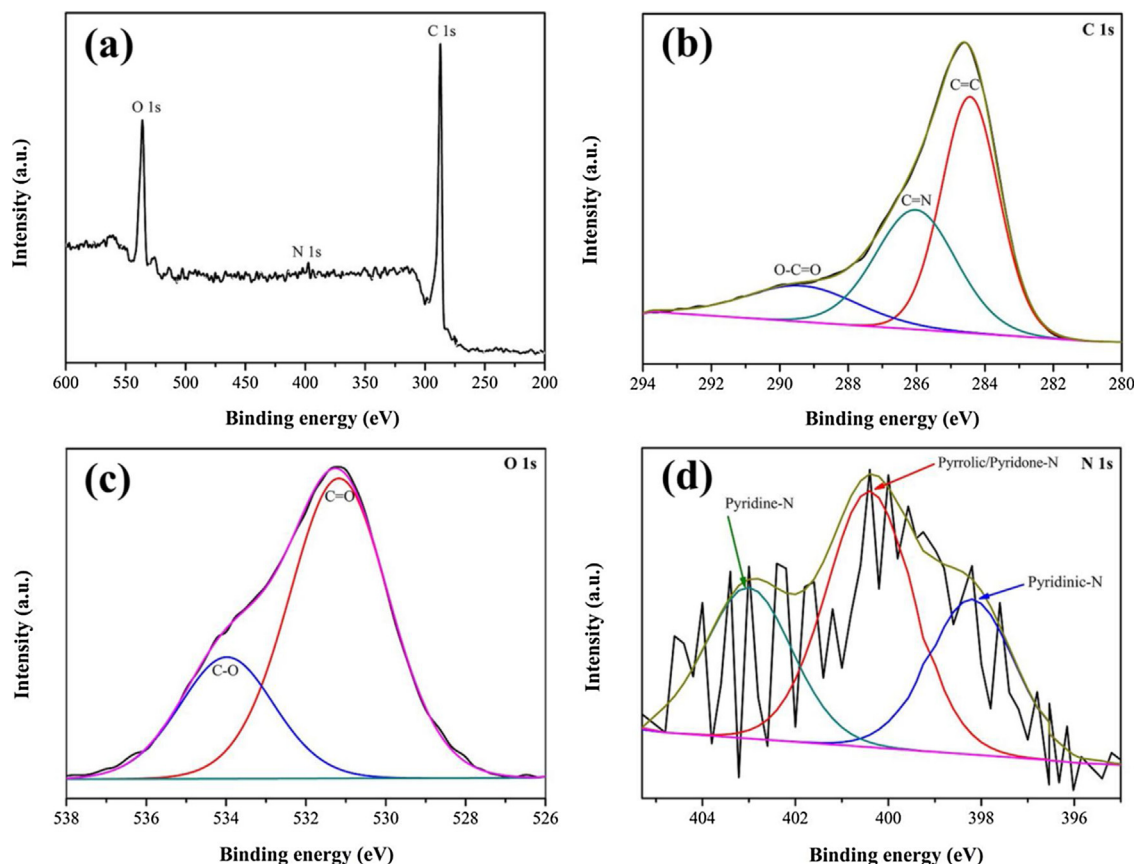
Fig. 7. XPS survey spectrum (a), high-resolution C 1s (b), O 1s (c), and N 1s (d) spectra for SAC-4.

confirm the reversible charging-discharging processes consistent with the aforementioned CV results, which is the characteristic of an ideal capacitor. The specific capacitance decreases with increasing current density, as shown in Fig. 8e, which can be attributed to the slow diffusion and migration of protons through the electrodes [36]. On the other hand, SAC-4 exhibits much higher specific capacitance than other materials, and 66.2% of the initial capacitance can be maintained in SAC-4 at a current density of $50 \, A \, g^{-1}$. The excellent electrochemical performance of SAC-4 is attributed to the unique 3D hierarchical network with fully interconnected nanostructure, which generates a large accessible surface area and creates short pathways for ion/electron transport [37].

The electrochemical impedance spectra for the electrode materials are depicted in Fig. 8f. It is known that Nyquist plots mainly include three parts: A semicircle in the high-frequency region, a straight line with a slope of 45° in the low-frequency region and a straight line with a slope larger than 45° in very low frequency region. As shown in the inset of Fig. 8f, the semicircle starting from the crossover point at Z_0 axis indicates the equivalent series resistance (Rs), and the semicircle diameter represents the charge transport resistance (Rct) at the electrode/electrolyte interfaces. It is clearly seen that the intercept of Z_0 axis is in the following order: SC (1.32 O) > SAC-0.5 (0.9 O) > SAC-8 (0.85 O) > SAC-2 (0.78 O) > SAC-6 (0.80 O) > SAC-4 (0.72 O). Meanwhile, SAC-4 exhibits a smaller diameter semicircle (about 0.07 O) than the others. Those results indicate that SAC-4 has lower solution resistance due to its unique pore structure and fast electrolyte transportation in the electrode materials. In addition, the straight line with a slope of nearly 45° for SAC-4 also suggests a fast charge diffusion and storage process in the electrode materials [26,38,39].

3.2.2. Electrochemical performance in the two-electrode system

SAC-4 exhibits the best capacitive performance in the aforementioned three-electrode system. Its electrochemical properties are further investigated in a two-electrode system. Fig. 9a displays the CV curves for SAC-4 symmetric supercapacitor operated in different voltage windows at $50 \, mV \, s^{-1}$. It is clearly seen that the supercapacitor can be reversibly cycled within the voltage window of 0–1.6 V. The CV curves for the symmetric supercapacitor are further illustrated in Fig. 9b, which exhibit a rectangular shape at sweep rates of 5, 10, 20 and $100 \, mV \, s^{-1}$. The GCD curves for SAC-4 show a nearly symmetrical triangle shape and still maintain the triangle shape at a current density as high as $10 \, A \, g^{-1}$ (Fig. 9c), which implies the ideal capacitive behavior of the sample. In addition, no obvious IR drop is observed even at high current densities, indicating its high charge-discharge efficiency and low internal resistance due to fast charge transfer and ion diffusion [39].

Fig. 9d summarizes the specific capacitances of SAC-4 at $0.2–10 \, A \, g^{-1}$. Even if the charge-discharge is at a current density as high as $10 \, A \, g^{-1}$, SAC-4 still maintains about 43.5% of its initial capacitance, while the decrease could be attributed to the diffusion and migration of less protons through the electrodes because of the high current density and limited volume. Fig. 9e shows the Ragone plots for SAC-4 in the two-electrode system. The energy density of the system is $16.1 \, Wh \, kg^{-1}$ at a power density of $160.0 \, W \, kg^{-1}$, which is higher than those of previously reported symmetric supercapacitors with electrode materials of biomass-derived carbon in aqueous electrolyte, such as porous carbons derived from lotus root shell ($13.9 \, Wh \, kg^{-1}$ at $6.4 \, kW \, kg^{-1}$) [40], shrimp shells ($5.2 \, Wh \, kg^{-1}$ at $1162 \, W \, kg^{-1}$) [41], and waste coffee beans ($10 \, Wh \, kg^{-1}$ at $6000 \, W \, kg^{-1}$) [42]. As shown in Fig. 9f, the Nyquist plot for SAC-4 possesses a steep slope of the curve and a
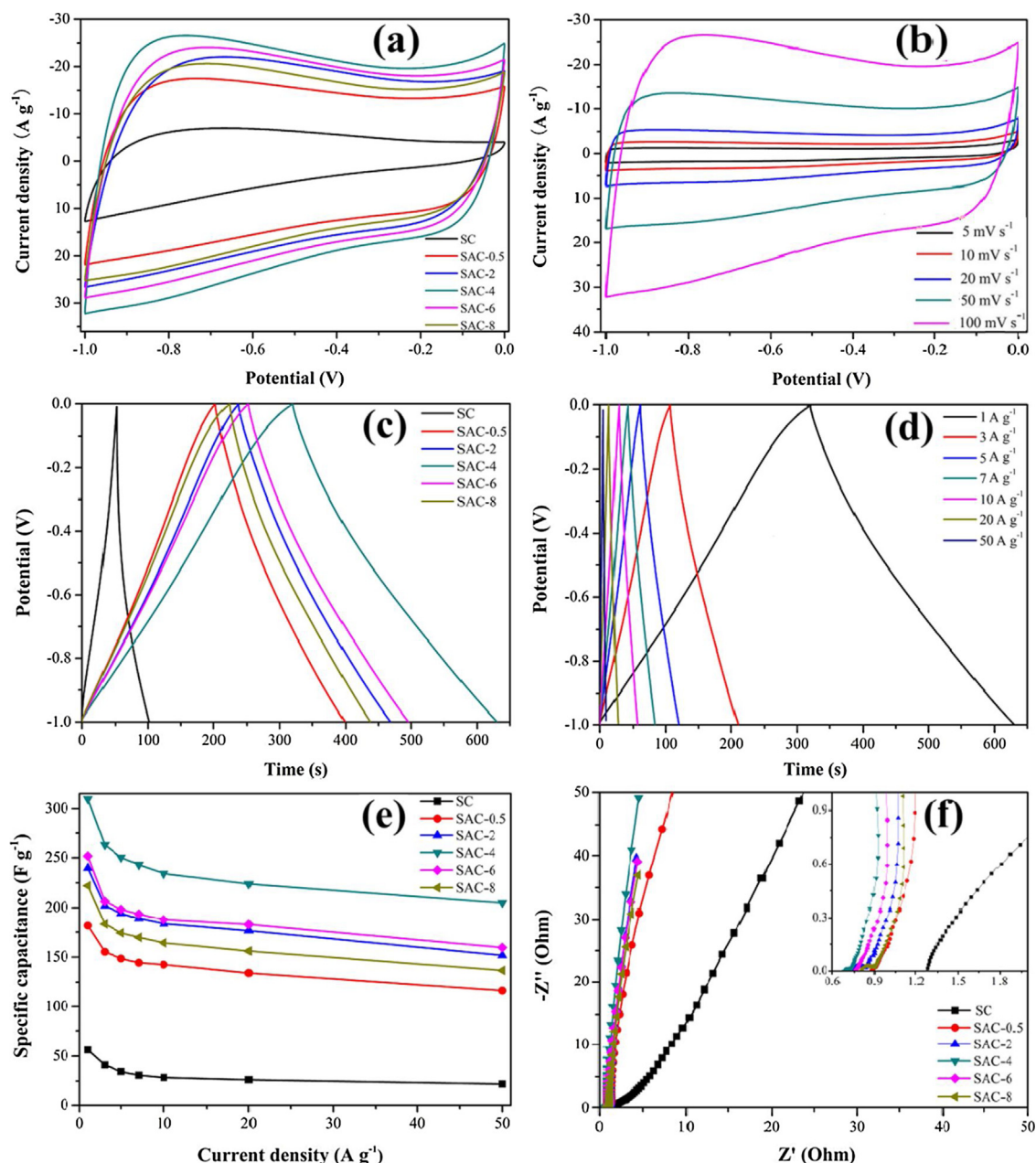
Fig. 8. Electrochemical performance of SC and SAC-*x* in a three-electrode system: (a) CV curves for SC and SAC-*x* at 100 mV s^{-1}; (b) CV curves for SAC-4 at various scan rates; (c) GCD curves for SC and SAC-*x* at 3 A g^{-1}; (d) GCD curves for SAC-4 at various current densities; (e) Specific capacitances of SC and SAC-*x* at different current densities; (f) Nyquist plots for SC and SAC-*x*.

semicircle with small diameter, suggesting the much reduced ion diffusion resistance of the electrode material. The interpretation of Nyquist diagram for the SAC-4-based symmetric supercapacitor also confirms SAC-4 is an ideal electrode material for supercapacitors (Fig. S2, Supplementary material).

Cycle stability is an important factor to characterize the materials for practical applications. The cycling performance and columbic efficiency of the SAC-4 electrode evaluated at 1 A g^{-1} are shown in Fig. 9g. Approximately, 81.3% capacitance retention and 100% columbic efficiency are obtained after 10,000 charge-discharge cycles, indicating the excellent cycling stability and good rate capability of SAC-4 electrode.

As discussed above, the excellent capacitive performance of SAC-4 could be related with the following factors: First, its high specific surface area and abundant micropores allow for the accumulation of more electrolyte ions and the increase in the effective

contact areas of electrode/electrolyte interfaces. Second, the hierarchical porous structure offers plentiful channels to facilitate the penetration of electrolytic ions even at high current densities. Third, the existence of N and O-containing surface functional groups can increase the electrical conductivity and wettability of electrodes [43–46]. Therefore, combined with its low cost and rich source, the loofah sponge-derived porous carbon materials are expected to become a superior electrode material for supercapacitor applications.

4. Conclusions

Low-cost and readily available loofah sponges are used as raw materials to prepare a series of porous activated carbon whose porous characteristics are controllable by changing the dosage of chemical etching reagent (KOH). The optimized carbon material
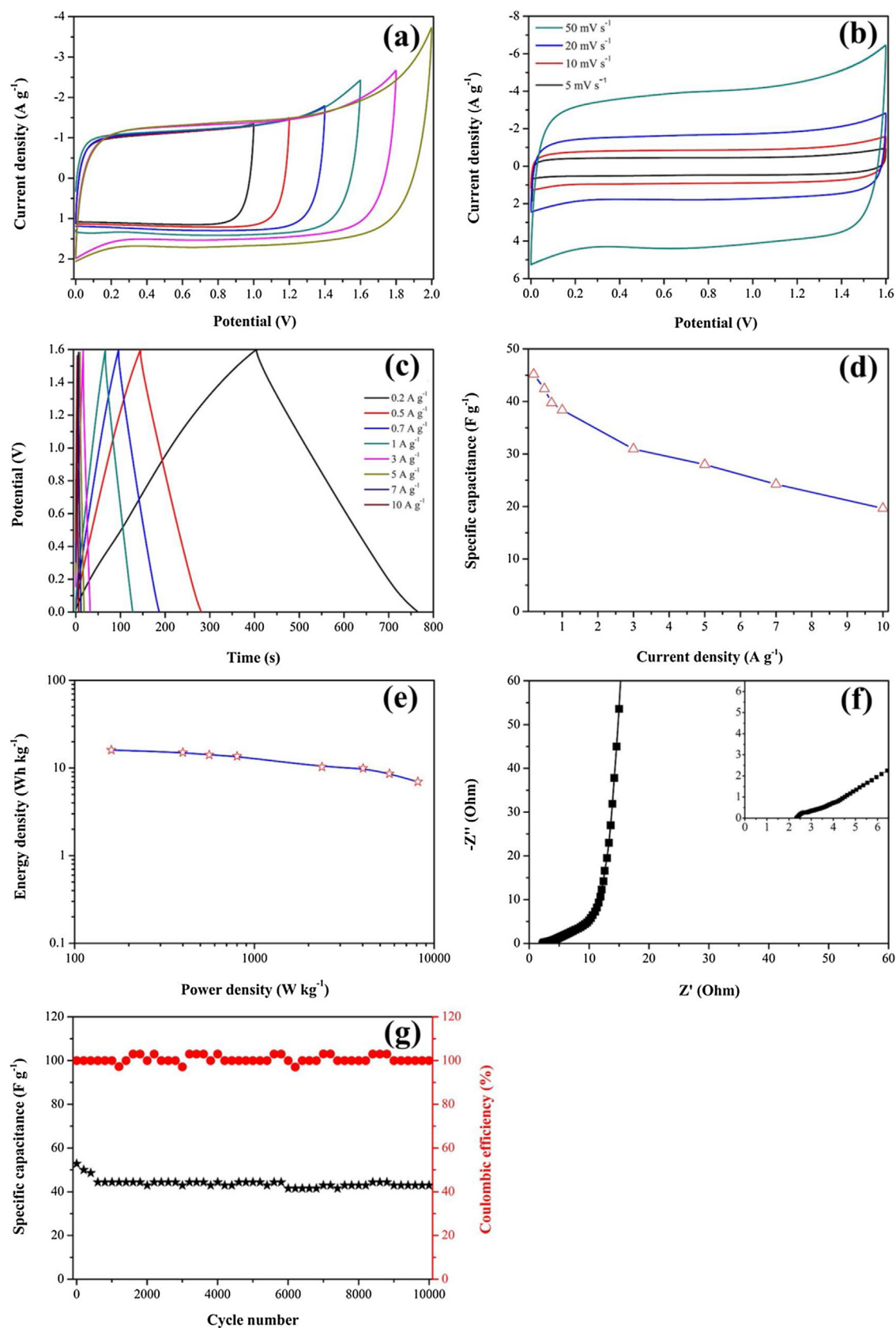
Fig. 9. Electrochemical performance of SAC-4 in a two-electrode system: (a) CV curves at $50\,mV\,s^{-1}$; (b) CV curves at various scan rates; (c) GCD curves at different current densities; (d) Specific capacitance at different current densities; (e) Nyquist plots; (f) The Ragone plots; and (g) The specific capacitance and columbic efficiency at $1\,A\,g^{-1}$.

denoted as SAC-4 exhibits a high specific capacitance of $309.6\,F\,g^{-1}$ at $1\,A\,g^{-1}$ in a three-electrode system with $6\,M$ KOH electrolyte. More importantly, the symmetric supercapacitor based on the SAC-4 electrode shows a high energy density of $16.1\,Wh\,kg^{-1}$ at a power density of $160.0\,W\,kg^{-1}$ with $1\,M\,Na_2SO_4$ electrolyte. The results demonstrate that the excellent capacitive performances of electrodes based on loofah sponge-derived porous carbon materials are attributed to their unique hierarchical porous structures and the heteroatom functionalities. It is expected that loofah sponge-derived porous carbon materials are of exciting commercial potential for supercapacitor applications.

Acknowledgements

Appendix A.　Supplementary data

Supplementary material related to this article can be found, in the online version, at doi:https://doi.org/10.1016/j.apsusc.2017.11.249

References

[1] V.D. Nithya, N.S. Arul, Review on α-Fe$_2$O$_3$ based negative electrode for high performance supercapacitors, J. Power Source 327 (2016) 297–318.

[2] P. Simon, Y. Gogotsi, Materials for electrochemical capacitors, Nat. Mater. 7 (2008) 845–854.

[3] A. Ehsani, E. Kowsari, M.D. Najafi, R. Safari, H.M. Shiri, Enhanced pseudocapacitive performance of electroactive p-type conductive polymer in the presence of 1-octadecyl-3-methylimidazolium bromide, J. Colloid Interface Sci. 503 (2017) 10–16.

[4] A. Afzal, F.A. Abuilaiwi, A. Habib, M. Awais, S.B. Waje, M.A. Atieh, Polypyrrole/carbon nanotube supercapacitors: technological advances and challenges, J. Power Source 352 (2017) 174–186.

[5] J. Liang, Y. Chai, D.L. Li, M. Li, J.X. Lu, L. Li, M. Luo, Facile fabrication of plate-shaped hydrohausmannite as electrode material for supercapacitors, Appl. Surf. Sci. 414 (2017) 68–72.

[6] P. Venkateswarlu, E. Umeshbabu, U.N. Kumar, P. Nagaraja, P. Tirupathi, G.R. Rao, P. Justin, Facile hydrothermal synthesis of urchin-like cobalt manganese spinel for high-performance supercapacitor applications, J. Colloid Interface Sci. 503 (2017) 17–27.

[7] X.Y. Zhao, X.L. Li, Y.J. Zhao, Z.L. Su, Y.Y. Zhang, R.H. Wang, Facile synthesis of Tremelliform Co$_{0.85}$Se nanosheets for supercapacitor, J. Alloy Compd. 697 (2017) 124–131.

[8] N.S. Wu, J.X. Low, T. Liu, J.G. Yu, S.W. Cao, Hierarchical hollow cages of Mn-Co layered double hydroxide as supercapacitor electrode materials, Appl. Surf. Sci. 413 (2017) 35–40.

[9] H.L. Cao, N.N. Wu, Y.Z. Liu, S.Y. Wang, W.J. Du, J.R. Liu, Facile synthesis of rod-like manganese molybdate crystallines with two-dimensional nanoflakes for supercapacitor application, Electrochim. Acta 225 (2017) 605–613.

[10] Y.Q. Liao, Y.L. Huang, D. Shu, Y.Y. Zhong, J.N. Hao, C. He, J. Zhong, X.N. Song, Three-dimensional nitrogen-doped graphene hydrogels prepared via hydrothermal synthesis as high-performance supercapacitor materials, Electrochim. Acta 194 (2016) 136–142.

[11] H.J. An, N.R. Kim, M.Y. Song, Y.S. Yun, H.J. Jin, Fallen-leaf-derived microporous pyropolymers for supercapacitors, J. Ind. Eng. Chem. 45 (2017) 223–228.

[12] C.C. Gong, X.Z. Wang, D.L. Ma, H.F. Chen, S.S. Zhang, Z.X. Liao, Microporous carbon from a biological waste-stiff silkworm for capacitive energy storage, Electrochim. Acta 220 (2016) 331–339.

[13] Q.F. Meng, K.F. Cai, Y.X. Chen, L.D. Chen, Research progress on conducting polymer based supercapacitor electrode materials, Nano Energy 36 (2017) 268–285.

[14] L.L. Xie, G.H. Sun, F.Y. Su, X.Q. Guo, Q.Q. Kong, X.M. Li, X.H. Huang, L. Wan, W. Song, K.X. Li, C.X. Lv, C.M. Chen, Hierarchical porous carbon microtubes derived from willow catkins for supercapacitor applications, J. Mater. Chem. A 4 (2017) 1637–1646.

[15] J. Sodtipinta, C. Ieosakulrat, N. Poonyayant, P. Kidkhunthod, N. Chanlek, T. Amornsakchai, P. Pakawatpanurut, Interconnected open-channel carbon nanosheets derived from pineapple leaf fiber as a sustainable active material for supercapacitors, Ind. Crops Prod. 104 (2017) 13–20.

[16] C.L. Long, L.L. Jiang, X.L. Wu, Y.T. Jiang, D.R. Yang, C.K. Wang, T. Wei, Z.J. Fan, Facile synthesis of functionalized porous carbon with three-dimensional interconnected pore structure for high volumetric performance supercapacitors, Carbon 93 (2015) 412–420.

[17] D. Xie, X.H. Xia, W.J. Tang, Y. Zhong, Y.D. Wang, D.H. Wang, X.L. Wang, J.P. Tu, Novel carbon channels from loofah sponge for construction of metal sulfide/carbon composites with robust electrochemical energy storage, J. Mater. Chem. A 5 (2017) 7578–7585.

[18] X.X. Gu, C.J. Tong, S. Rehman, L.M. Liu, Y.L. Hou, S.Q. Zhang, Multifunctional nitrogen-doped loofah sponge carbon blocking layer for high performance rechargeable lithium batteries, ACS Appl. Mater. Interface 8 (2016) 15991–16001.

[19] Y.T. Luan, L. Wang, S.E. Guo, B.J. Jiang, D.D. Zhao, H.J. Yan, C.G. Tian, H.G. Fu, A hierarchical porous carbon material from a loofah sponge network for high performance supercapacitors, RSC Adv. 5 (2015) 42430–42437.

[20] Z.C. Li, K.L. Zhai, G.Q. Wang, Q. Li, P.Z. Guo, Preparation and electrocapacitive properties of hierarchical porous carbons based on loofah sponge, Materials 9 (2016) 912.

[21] Y.T. Luan, Y.Q. Huang, L. Wang, M.X. Li, R.H. Wang, B.J. Jiang, Porous carbon@MnO$_2$ and nitrogen-doped porous carbon from carbonized loofah sponge for asymmetric supercapacitor with high energy and power density, J. Electroanal. Chem. 763 (2016) 90–96.

[22] X.L. Su, M.Y. Cheng, L. Fu, J.H. Yang, X.C. Zheng, X.X. Guan, Superior supercapacitive performance of hollow activated carbon nanomesh with hierarchical structure derived from poplar catkins, J. Power Sources 362 (2017) 27–38.

[23] Y. Teng, E.H. Liu, R. Ding, K. Liu, R.H. Liu, L. Wang, Z. Yang, H.X. Jiang, Bean dregs-based activated carbon/copper ion supercapacitors, Electrochim. Acta 194 (2016) 394–404.

[24] K. Wang, N. Zhao, S.W. Lei, R. Yan, X.D. Tian, J.Z. Wang, Y. Song, D.F. Xu, Q.G. Guo, L. Liu, Promising biomass-based activated carbons derived from willow catkins for high performance supercapacitors, Electrochim. Acta 166 (2015) 1–11.

[25] B. Liu, H.B. Chen, Y. Gao, H.M. Li, Preparation and capacitive performance of porous carbon materials derived from eulaliopsis binate, Electrochim. Acta 189 (2016) 93–100.

[26] D.Y. Lee, G.H. An, H.J. Ahn, High-surface-area tofu based activated porous carbon for electrical double-layer capacitors, J. Ind. Eng. Chem. 52 (2017) 121–127.

[27] B. Duan, X. Gao, X. Yao, Y. Fang, L. Huang, J. Zhou, L.N. Zhang, Unique elastic N-doped carbon nanofibrous microspheres with hierarchical porosity derived from renewable chitin for high rate supercapacitors, Nano Energy 27 (2016) 482–491.

[28] T.Y. Wei, X.L. Wei, Y. Gao, H.M. Li, Large scale production of biomass-derived nitrogen-doped porous carbon materials for supercapacitors, Electrochim. Acta 169 (2015) 186–194.

[29] X.Y. Zhou, H.C. Li, J. Yang, Biomass-derived activated carbon materials with plentiful heteroatoms for high-performance electrochemical capacitor electrodes, J. Energy Chem. 25 (2016) 35–40.

[30] D.C. Liu, W.L. Zhang, H.B. Lin, Y. Li, H.Y. Lu, Y. Wang, A green technology for the preparation of high capacitance rice husk-based activated carbon, J. Clean. Prod. 112 (2016) 1190–1198.

[31] H.B. Feng, H. Hu, H.W. Dong, Y. Xiao, Y.J. Cai, B.F. Lei, Y.L. Liu, M.T. Zheng, Hierarchical structured carbon derived from bagasse wastes: a simple and efficient synthesis route and its improved electrochemical properties for high-performance supercapacitors, J. Power Sources 302 (2016) 164–173.

[32] G.F. Ma, Q. Yang, K.J. Sun, H. Peng, F.T. Ran, X.L. Zhao, Z.Q. Lei, Nitrogen-doped porous carbon derived from biomass waste for high-performance supercapacitor, Bioresource Technol. 197 (2015) 137–142.

[33] C.S. Wang, T.Z. Liu, N. Nori-based, O, S, Cl co-doped carbon materials by chemical activation of ZnCl$_2$ for supercapacitor, J. Alloy Compd. 696 (2017) 42–50.

[34] Y. Fan, P.F. Liu, B. Zhu, S.F. Chen, K.L. Yao, R. Han, Microporous carbon derived from acacia gum with tuned porosity for high-performance electrochemical capacitors, Int. J. Hydrogen Energy 40 (2015) 6188–6196.

[35] Z. Li, L. Zhang, B.S. Amirkhiz, X.H. Tan, Z.W. Xu, H.L. Wang, B.C. Olsen, C.M.B. Holt, D. Mitlin, Carbonized chicken eggshell membranes with 3D architectures as high-performance electrode materials for supercapacitors, Adv. Energy Mater. 2 (2012) 431–437.

[36] P. Cheng, S.Y. Gao, P.Y. Zang, X.F. Yang, Y.L. Bai, H. Xu, Z.H. Liu, Z.B. Lei, Hierarchically porous carbon by activation of shiitake mushroom for capacitive energy storage, Carbon 93 (2015) 315–324.

[37] C.J. Yuan, H.B. Lin, H.Y. Lu, E.D. Xing, Y.S. Zhang, B.Y. Xie, Synthesis of hierarchically porous MnO$_2$/rice husks derived carbon composite as high-performance electrode material for supercapacitors, Appl. Energy 178 (2016) 260–268.

[38] L. Chen, T. Ji, L.W. Mu, J.H. Zhu, Cotton fabric derived hierarchically porous carbon and nitrogen doping for sustainable capacitor electrode, Carbon 11 (2017) 839–848.

[39] Y.J. Li, G.L. Wang, T. Wei, Z.J. Fan, P. Yan, Nitrogen and sulfur co-doped porous carbon nanosheets derived from willow catkin for supercapacitors, Nano Energy 19 (2016) 165–175.

[40] X. Wang, M.J. Wang, X.M. Zhang, H.J. Li, X.H. Guo, Low-cost, green synthesis of highly porous carbons derived from lotus root shell as superior performance electrode materials in supercapacitor, J. Energy Chem. 25 (2016) 26–34.

[41] J.Y. Qua, C. Geng, S.Y. Lv, G.H. Shao, S.Y. Ma, M.B. Wu, Nitrogen, oxygen and phosphorus decorated porous carbons derived from shrimp shells for supercapacitors, Electrochim. Acta 176 (2015) 982–988.

[42] T.E. Rufford, D. Hulicova-Jurcakova, Z.H. Zhu, G.Q. Lu, Nanoporous carbon electrode from waste coffee beans for high performance supercapacitors, Electrochem. Commun. 10 (2008) 1594–1597.

[43] D.B. Wang, Z. Geng, B. Li, C. Zhang, High performance electrode materials for electric double-layer capacitors based on biomass-derived activated carbons, Electrochim. Acta 173 (2015) 377–384.

[44] C. Chen, D.F. Yu, G.Y. Zhao, B.S. Du, W. Tang, L. Sun, Y. Sun, F. Besenbacher, M. Yu, Three-dimensional scaffolding frame work of porous carbon nanosheets derived from plant wastes for high-performance supercapacitors, Nano Energy 27 (2016) 377–389.

[45] M. Zhang, X. Jin, L.N. Wang, M.J. Sun, Y. Tang, Y.M. Chen, Y.Z. Sun, X.J. Yang, P.Y. Wan, Improving biomass-derived carbon by activation with nitrogen and cobalt for supercapacitors and oxygen reduction reaction, Appl. Surf. Sci. 411 (2017) 251–260.

[46] A. Jain, C.H. Xu, S. Jayaraman, R. Balasubramanian, J.Y. Lee, M.P. Srinivasan, Mesoporous activated carbons with enhanced porosity by optimal hydrothermal pre-treatment of biomass for supercapacitor applications, Micropor. Mesopor. Mat. 218 (2015) 55–61.